Characterization of wetting using topological principles

Chenhao Sun[a], James E. McClure[b], Peyman Mostaghimi[a], Anna L. Herring[c], Douglas E. Meisenheimer[d], Dorthe Wildenschild[d], Steffen Berg[e,f,g] and Ryan T. Armstrong[a,*]

[a]*School of Minerals & Energy Resources Engineering, University of New South Wales, Kensington, NSW 2052, Australia*

[b]*Advanced Research Computing, Virginia Polytechnic Institute & State University, Blacksburg, Virginia 24061, USA*

[c]*Department of Applied Mathematics, Australian National University, Canberra, ACT 2601, Australia*

[d]*Department of Chemical, Biological and Environmental Engineering, Oregon State University, Corvallis, Oregon 97331, USA*

[e]*Hydrocarbon Recovery, Shell Global Solutions International B.V., Grasweg 31, 1031 HW Amsterdam, The Netherlands*

[f]*Department of Earth Science & Engineering, Imperial College London, London SW7 2AZ, UK*

[g]*Department of Chemical Engineering, Imperial College London, London SW7 2AZ, UK*

ABSTRACT

Hypothesis

Understanding wetting behavior is of great importance for natural systems and technological applications. The traditional concept of contact angle, a purely geometrical measure related to curvature, is often used for characterizing the wetting state of a system. It can be determined from Young's equation by applying equilibrium thermodynamics. However, whether contact angle is a representative measure of wetting for systems with significant complexity is unclear. Herein, we hypothesize that topological principles based on the Gauss-Bonnet theorem could yield a robust measure to characterize wetting.

Theory and Experiments

We introduce a macroscopic contact angle based on the deficit curvature of the fluid interfaces that are imposed by contacts with other immiscible phases. We perform sessile droplet simulations followed by multiphase experiments for porous sintered glass and Bentheimer sandstone to assess the sensitivity and robustness of the topological approach and compare the results to other traditional approaches.

Findings

We show that the presented topological principle is consistent with thermodynamics under the simplest conditions through a variational analysis. Furthermore, we elucidate that at sufficiently high image resolution the proposed topological approach and local contact angle measurements are comparable. While at lower resolutions, the proposed approach provides more accurate results being robust to resolution-based effects. Overall, the presented concepts open new pathways to characterize the wetting state of complex systems and theoretical developments to study multiphase systems.

1. Introduction

The inherent property of wetting refers to the preferential affinity of a fluid that is immersed in another immiscible fluid to coat a solid material [1, 2, 3]. Due to the ubiquitous existence of colloidal and interfacial phenomena in nature and applications, understanding the role of wetting is a key principal of interest. This intriguing interest in wetting behavior is motivated by numerous advanced technologies in nanotechnology, biological engineering, material science and geosciences [4, 5, 6, 7]. For instance, the design of bio-inspired fluidics, directional fluid transportation, composite functional materials, nano/micro-fluidics and energy storage systems require a precise and effective way to describe the wetting state therein.

Since 1805, Young's equation, based on thermodynamic laws, is firmly established to infer the wettability of a flat and chemically homogeneous solid surface at equilibrium [8], $\cos \theta_Y = \frac{\sigma_{ls}-\sigma_{vs}}{\sigma_{lv}}$, where the subscripts denote the immiscible fluids (liquid l and vapor v) and solid (s) for the associated surface free energies. θ_Y is the contact angle formed at the microscopic contact point on the surface, as depicted in Fig. 1. Wetting hysteresis due to the contribution of surface heterogeneity and contact line dynamics has been studied in detail over the last century [9, 10, 11]. However, despite theoretical and experimental investigations through the last 70 years [1, 2, 12, 13, 14, 15], several fundamental challenges in characterizing wetting state of complex multiphase systems remain unsolved and are currently pending.

For disordered and complex porous geometries ranging from catalysts in fuel cells to lungs in the respiratory system to porous glass filters to subsurface rocks, there are multiple length scales, various surface free energies, and surface heterogeneity involved. The convoluted interplay of physicochemical properties with multi-scale complexities therein presents significant spatial variability of contact angles along the three-phase contact line [16, 17], which leads to the resulting wetting hysteresis behavior and pinning effects. Accordingly, these features trigger a formidable challenge to

*Corresponding author

✉ E-mail address: ryan.armstrong@unsw.edu.au (R.T. Armstrong)
ORCID(s):

characterizing wetting behavior, which are far from being solved. It is therefore controversial whether Young's law is still applicable for these disordered and complex solids [18].

In the past, contact angle (and curvature) measurements were mainly based on two-dimensional (2D) projections, and in configurations that are optically transparent such as a typical sessile drop setup [19]. However, three-dimensional (3D) imaging provides the possibility to determine contact angles within opaque porous media [20, 21, 22, 23]. Possible 3D imaging technologies are 3D X-ray microcomputed tomography (micro-CT) [24] and confocal microscopy [25]. Given the rapid developments in 3D imaging technologies, there is an opportunity for interface science to make use of this methodology where the wetting of various porous domains would be of interest. The first community that started adopting this new technology is the porous media community, out of pure necessity to measure the wettability of immiscible fluids in geological materials, which are naturally opaque [26, 27, 28]. These efforts rely on micro-CT images of porous rocks saturated with immiscible phases [24]. The image voxels of a 3D system are segmented into respective phases [29] followed by the identification of the three-phase contact line to measure spatially distributed apparent contact angles, θ_{app}, for each microscopic three-phase contact point along the contact line. As shown in the right side of Fig. 1, the method measures the angle between the local tangential plane of liquid/vapor interface and the solid surface in the vicinity of three-phase contact points. Thus, the approach represents *in situ* θ_{app} directly along the contact line, which refers to microscopic wetting. However, the simplicity of θ_{app} computed by the local method is susceptible to errors due to image quality and pixelation-related segmentation errors [30, 31]. In particular, the identification of the three-phase contact line and measurement of an angle over a few voxels is inherently error-prone, as will be investigated herein. Ultimately, these systematic errors complicate the process of quantifying the wetting state of a porous multiphase system.

Another issue arises by using for the purpose of wetting characterization the concept of contact angle, which is subject to hysteresis. Due to hysteresis that is emphasized by complex geometries, surface heterogeneity, and interface dynamics, it is very questionable whether contact angle is a representative measure for characterizing wetting in such systems [9, 10, 32, 33, 34]. In addition, the line tension and disjoining/cojoining pressure occur along the contact line. Contact line tension, which is the excess free energy per unit length, is a dominant parameter in microscopic wetting [35]. It contributes to intermolecular force balance, resulting in contact line pinning and the associated hysteresis loop of contact angles [1, 2, 3]. Therefore, the variations on contact line curvature and the associated θ_{app} vary from a microscopic point of view due to the effects of surface heterogeneity and flow dynamics, which yields unexpected wetting behavior. Despite these parameters influencing microscopic wetting and hysteresis behavior, the question arises as to whether θ_{app} can capture enough information to rep-
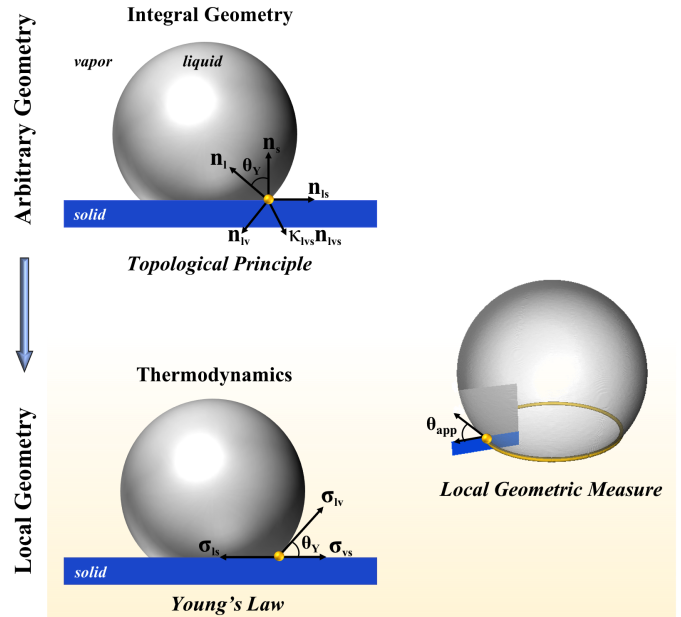

Fig. 1: The schematic illustration of topological principle based on integral geometry [16] and Young's equation based on thermodynamics at a microscopic contact point when a sessile droplet is deposited on a flat solid substrate exposed to vapor phase. The schematic illustration of apparent contact angle θ_{app} extraction by local measurement along the contact line.

resent the wetting state of the system and provide sufficient guidance for the design of functional surfaces?

Previous studies demonstrate that θ_{app} alone provides an incomplete description of wetting where the contact line is asymmetric [36]; especially for characterizing the macroscopic wetting behavior of multiphase systems, which has remained unexplored from a theoretical perspective. The wetting behavior synergistic affects on the phase topology and contact area with the solid surface, which must also be considered. It can be representative of the macroscopic wetting of the system and captures the complete microscopic information related to the thermodynamics. To this end, in our previous works [37, 16], we developed a theory based on topological principles that can effectively describe wetting behavior, which links across various length scales pertinent to wetting phenomena. Herein, we aim to quantitatively and qualitatively unravel the effective and robust nature of the proposed theory by providing in-depth analysis and comparison to other recent methods for characterizing the wettability of multiphase systems.

2. Theoretical Concepts

2.1. Deficit Curvature from Gaussian Curvature

Topological principle is applied to characterize the wetting state of a given multiphase system by the link of the Gauss-Bonnet theorem. For a fluid droplet D that has a closed interface in the three-phase system, where liquid (l), vapor (v) and solid (s) are present, the total curvature of the

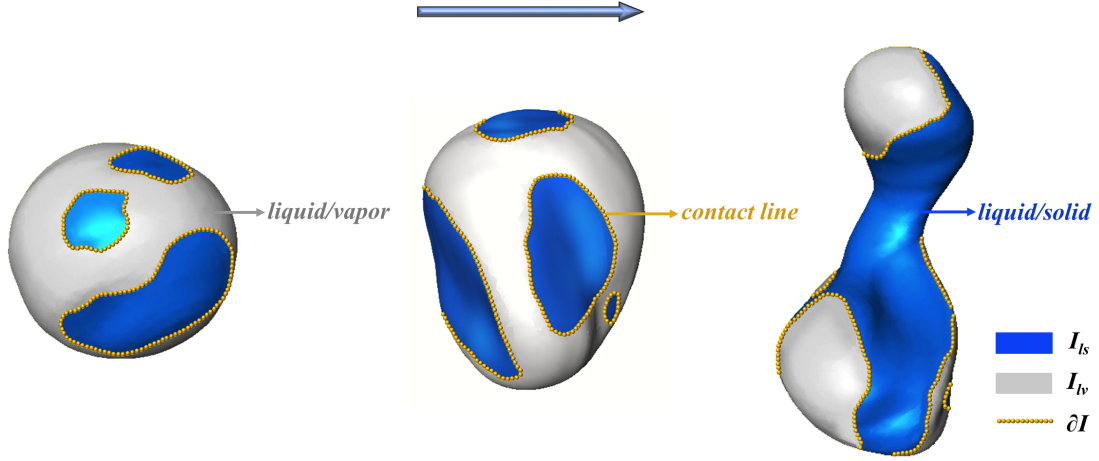**Increasing Complexity of Droplet Morphology**

Fig. 2: Schematic diagram of 3D droplets on contact with a complex solid (transparent) with labeled definitions where grey color denotes the liquid/vapor interface (I_{lv}), and blue color denotes the liquid/solid interface (I_{ls}). The contact line loops are formed by three-phase contact points (yellow circles). From left to right, there is an increasing complexity of droplet morphology.

fluid surface and its global topology are related by the Gauss-Bonnet theorem [38, 37]. As a consequence, the Euler characteristic χ and its total curvature for the surface I of the droplet D obey the following expression,

$$2\pi\chi(D) = \int_I \kappa_G dA + \int_{\partial I} \kappa_g dC, \qquad (1)$$

where dA and dC are the droplet interfacial area element along the surface I and the line element along the contact line ∂I, respectively. κ_G and κ_g are Gaussian curvature along the droplet interface and geodesic curvature along the contact line ∂I, respectively.

For a 3D droplet, we can arrive at a generalized form of the expression by subdividing the fluid surface into liquid/vapor (lv) and liquid/solid (ls) interfaces,

$$4\pi\chi(D) = 2\pi\chi(I_{lv}) + 2\pi\chi(I_{ls})$$
$$= \int_{I_{lv}} \kappa_G dA + \int_{I_{ls}} \kappa_G dA + \int_{\partial I} (\kappa_{g_{lv}} + \kappa_{g_{ls}}) dC. \qquad (2)$$

It indicates that the Euler characteristic of the droplet always remains constant and the geodesic curvature source term, $\int_{\partial I}(\kappa_{g_{lv}} + \kappa_{g_{ls}})dC$, will change accordingly based on the contribution of total surface curvature due to the wetting behavior of the system. The deficit curvature, Θ, is defined as the summation of geodesic curvatures along the contact line relative to the tangential plane for each interface and corresponds to a total angle of change. By considering a droplet deposited on a flat, smooth and homogeneous surface as shown in the top of Fig.1, Θ along the contact line

can be expressed by the labeled notations as,

$$\Theta = \int_{\partial I} (\kappa_{g_{lv}} + \kappa_{g_{ls}}) dC$$
$$= \int_{\partial I} \kappa_{lvs} \mathbf{n}_{lvs} \cdot \left[\mathbf{n}_s \sin\theta_Y + \mathbf{n}_{ls}(1 - \cos\theta_Y) \right] dC, \qquad (3)$$

where $\mathbf{n}_{lvs}$ is the normal vector to the contact line, which points in the direction of the curvature for the contact line. $\mathbf{n}_{lv}$ is the outward normal vector along the contact line relative to the droplet interface. $\mathbf{n}_{ls}$ is the outward normal vector along the contact line relative to the liquid/solid interface. From Eq. (3), it is evident that Θ obtained by applying the topological principle is an explicit average of intrinsic contact angle, i.e. Young's angle (θ_Y) for this situation. Therefore, Θ can be interpreted in terms of fluid morphology in a way that is not affected by the contact angle hysteresis due to surface heterogeneity, geometry complexity, and interface dynamics [16].

For solid surfaces that contain disordered and complex geometries or even with confined domains as shown in Fig. 2, we can revisit Eq. (2) to obtain Θ. Macroscopic contact angle θ_{macro} can be obtained by using a normalizing factor λ to scale the desired contact angle interval in $\theta_{macro} \in [0, \pi]$,

$$\theta_{macro} = \lambda\Theta$$
$$= \lambda \left[4\pi\chi(D) - \left(\int_{I_{lv}} \kappa_G dA + \int_{I_{ls}} \kappa_G dA \right) \right]. \qquad (4)$$

The nature of this formulation resolves a few pressing issues. Firstly, the angle along the contact line is not directly computed as an average from the sequence of local geometric contact angle point measurements. θ_{macro} is inferred from interfacial curvature and area measurements along with a topological measurement. While these measures are still

susceptible to pixelization effects, it is expected that these effects would be less than that resulting from local measurements along the three-phase contact line (as tested herein). Secondly, θ_{macro} accounts for the complete geodesic curvature of the contact line, which is the curvature of the three-phase contact line relative to both the solid surface and liquid/vapor interface. Therefore, the formulation captures wetting effects as evident by line tension and θ_{app}, which are both known to influence wetting behavior.

2.2. Derivation of Young's Equation

In this section, we show the direct link between the topological and thermodynamic concepts for determining the wetting state of the system by applying surface energy minimization and variational principles [39]. The Gauss-Bonnet theorem allows us to express the total curvature of a droplet D in terms of deficit curvature, corresponding average curvature and surface area,

$$4\pi\chi(D) = \Theta + \kappa_{lv}A_{lv} + \kappa_{ls}A_{ls} . \tag{5}$$

Here, we consider a variational principle of the internal energy as applied in thermodynamic approaches. The variation of the internal energy is given by Euler's homogeneous function theorem,

$$\delta U = T\delta S - p_v\delta V_v - p_l\delta V_l + \sigma_{lv}\delta A_{lv} \\ +\sigma_{ls}\delta A_{ls} + \sigma_{vs}\delta A_{vs} . \tag{6}$$

Based on this, we consider a closed system with $\delta U = 0$. Droplet rearrangements can occur provided that the volume is not changed, meaning that $\delta V_l = \delta V_v = 0$. Therefore, entropy production in the system is strictly linked to the minimization of the surface energy,

$$\delta S = -\frac{1}{T}\left[\sigma_{lv}\delta A_{lv} + \sigma_{ls}\delta A_{ls} + \sigma_{vs}\delta A_{vs}\right] \geq 0 . \tag{7}$$

The total surface area of the solid substrate is constant, then

$$\delta A_s = \delta A_{vs} + \delta A_{ls} = 0 , \tag{8}$$

which can be used to eliminate one of the surface areas from Eq. (7). The topological constraint from Eq. (5) determines the condition that should be imposed to ensure that geometric variation occurs without changing the topology,

$$\delta\left[4\pi\chi(D)\right] = \delta\Theta + \kappa_{lv}\delta A_{lv} + A_{lv}\delta\kappa_{lv} \\ \kappa_{ls}\delta A_{ls} + A_{ls}\delta\kappa_{ls} \tag{9} \\ = 0 .$$

We shall impose Eq. (9) as a constraint on Eq. (7) using the method of Lagrange multipliers, also using Eq. (8) to

eliminate A_{vs}. Now, we can express the entropy production as

$$\delta S = -\frac{1}{T}\left[\underbrace{\left(\sigma_{ls} - \sigma_{vs} + \frac{\sigma_{lv}\kappa_{ls}}{\kappa_{lv}}\right)\delta A_{ls}}_{\text{surface area variation}} \right. \\ \left. + \frac{\sigma_{lv}}{\kappa_{lv}}\underbrace{\left(\delta\Theta + A_{lv}\delta\kappa_{lv} + A_{ls}\delta\kappa_{ls}\right)}_{\text{total curvature variation}}\right] . \tag{10}$$

This expression separates terms associated with the variation of the surface area from terms that redistribute curvature along the cluster boundary. Put another way, the second term corresponds to a redistribution of the total curvature that occurs at constant surface area due to the deformation of the droplet. One of the ways to redistribute the total curvature is by altering the deficit curvature, which changes the contact angle. Since $T > 0$, the inequality can be re-expressed in the form,

$$\left(\frac{\sigma_{ls} - \sigma_{vs}}{\sigma_{lv}}\kappa_{lv} + \kappa_{ls}\right)\delta A_{ls} + \delta\Theta + A_{lv}\delta\kappa_{lv} + A_{ls}\delta\kappa_{ls} \leq 0 , \tag{11}$$

which is equivalent to stating that the surface energy of the system must decrease.

Since the solid surface is flat, which means $\kappa_{ls} = 0$ and $\delta\kappa_{ls} = 0$. The variations can be computed directly based on expressions for a spherical cap with droplet radius R and droplet height h to the solid surface, where

$$\Theta = 2\pi(1 - \cos\theta) \\ \kappa_{lv} = \frac{1}{R^2} \\ A_{lv} = 2\pi Rh \\ A_{ls} = \pi h(2R - h) \tag{12}$$

and the associated variations

$$\delta\Theta = \delta\left[2\pi(1 - \cos\theta)\right] = 2\pi(hR^{-2}\delta R - R^{-1}\delta h) \\ \delta\kappa_{lv} = \delta\left[R^{-2}\right] = -2R^{-3}\delta R \tag{13} \\ \delta A_{ls} = \delta\left[\pi h(2R - h)\right] = \pi\left(2h\delta R + 2R\delta h - 2h\delta h\right)$$

The volume of a spherical cap is $V = \frac{1}{3}\pi h^2(3R - h)$, and setting $\delta V = 0$ imposes the relationship $\delta R = \left(1 - \frac{2R}{h}\right)\delta h$. Inserting this into expressions above, we obtain

$$\delta\Theta = 2\pi\left(\frac{h}{R^2} - \frac{3}{R}\right)\delta h \\ \delta\kappa_{lv} = \left(\frac{4}{R^2h} - \frac{2}{R^3}\right)\delta h \tag{14} \\ \delta A_{ls} = -2\pi R\delta h$$

Inserting Eqs. (12) and (14) into Eq. (11) and rearranging terms gives

$$\frac{2\pi\delta h}{R}\left\{1 - \frac{h}{R} - \frac{\sigma_{cs} - \sigma_{as}}{\sigma_{ca}}\right\} \leq 0 . \qquad (15)$$

Noting that $\cos\theta = 1 - h/R$, we observe that for a general variation δh and $R > 0$, the entropy maximum will be obtained based on the condition

$$\cos\theta - \frac{\sigma_{ls} - \sigma_{vs}}{\sigma_{lv}} = 0 , \qquad (16)$$

which is Young's equation for the contact angle. The classical result is thereby obtained when the shape of the contact line is radially symmetric. This outcome provides evidence to demonstrate that the proposed topological concept is a general explicit geometric statement and also has a direct link to classical thermodynamics.

3. Computation of Macroscopic Contact Angle

Algorithm 1 Implementation in computation of macroscopic contact angles for droplets in multiphase system.

---

for each droplet in the system **do**
    2D surface manifold generation by marching cubes algorithm
    Gaussian smooth for the manifold:
    $v'_i = v_i + \alpha \sum w_{ij}(v_j - v_i)$
    for each triangle on the manifold **do**
        Compute triangle area:
        $A_i = \frac{1}{2}|v_{12} \times v_{13}|$
        Compute principal curvatures κ_1 and κ_2
        Compute Gaussian curvature:
        $\kappa_{Gi} = \kappa_1\kappa_2$
        Compute mean curvature:
        $\kappa_{Mi} = \frac{\kappa_1+\kappa_2}{2}$
        if $\kappa_M < 0$ **then**
            $\kappa_{Gi}A_i = -\kappa_{Gi}A_i$
        end if
    end for
    Compute θ_{macro} by normalizing deficit curvature with the number of contact line loop N:
    $\theta_{macro} = \lambda\Theta = \frac{4\pi - \sum \kappa_{Gi}A_i}{4N}$
end for

To explain the implementation of the proposed topological principle to characterize the wetting state of the system, we first chose a droplet in a complex and confined domain from the segmented image for illustration. By modeling the whole droplet surface manifold using a generalized marching cubes algorithm [40], we performed a triangular approximation of the interface for each region (e.g., liquid/vapor and liquid/solid) to preserve the droplet topology. To obtain
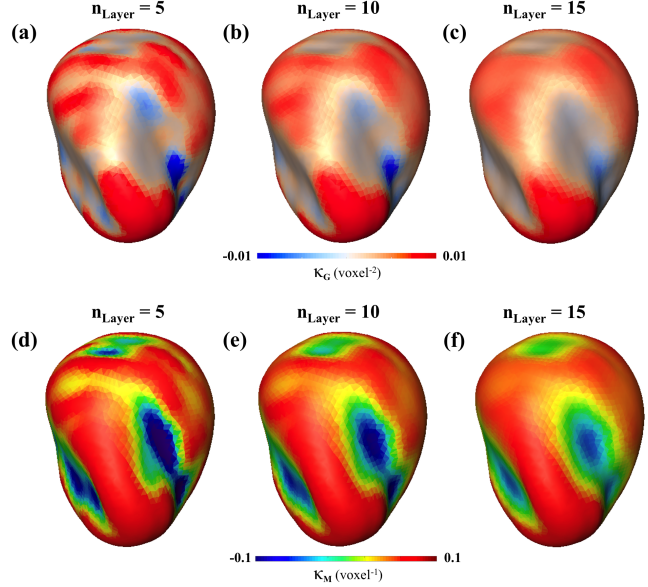

Fig. 3: The distribution of (a) - (c) Gaussian curvatures and (d) - (f) mean curvatures on the droplet interface for various degrees of n_{Layer}, which determines the number of triangles considered to be neighbours of a given point. Consequently, it determines the quadratic form equation of the surface patch. As the value of n_{Layer} increases, the number of the surrounding triangles to be considered as neighbours increases, which leads to more accurate results.

accurate results and remove extreme outliers of curvatures, a simplification of the triangles by applying an edge collapse algorithm for the droplet surface was required to omit small non-smooth regions. For instance, the small concave spots in the convex regions will be degenerated during the triangle contraction process. The area of each triangle A_i can be computed by the cross product of the two adjacent vectors (v_{12}, v_{13}) formed by the vertices $(v_1, v_2 \text{ and } v_3)$, which is $A_i = \frac{1}{2}|v_{12} \times v_{13}|$. Further, we smoothed the surface manifold by shifting its vertices to minimize the voxelization effects and segmentation errors. Each new vertex position (v'_i) was shifted towards the average position of its neighbours (v_j) by the weights (w_{ij}). Therefore, the vector average for the vertex can be obtained,

$$\Delta v_i = \sum w_{ij}(v_j - v_i), \qquad (17)$$

and the updated vertex position will be

$$v'_i = v_i + \alpha\Delta v_i, \qquad (18)$$

where α represents a scale factor ranging from 0 to 1. We then computed the magnitude and direction of the principal curvatures (κ_1 and κ_2) by fitting a quadratic form equation on the desired surface patch and obtaining its corresponding eigenvalues and eigenvectors [30]. The Gaussian curvature (κ_{Gi}) and mean curvature (κ_{Mi}) for each triangle can thereby
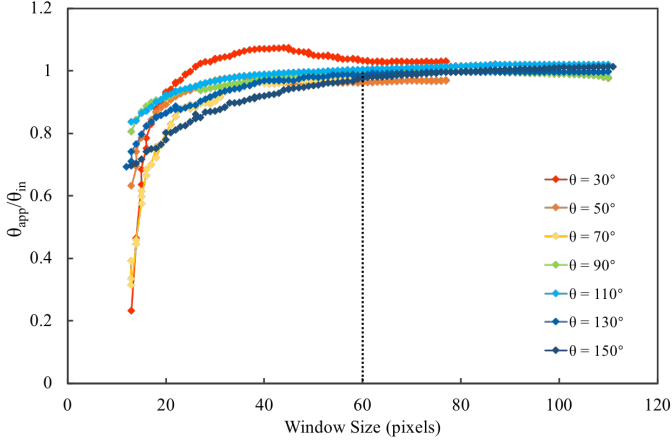
Fig. 4: Measured contact angles for different simulated droplets with increasing window size. It shows that an optimal window size of 60 pixels is sufficient to accurately measure the apparent contact angle by the 2D local method.

be obtained in terms of the principal curvatures,

$$\kappa_{Gi} = \kappa_1 \kappa_2,$$
$$\kappa_{Mi} = \frac{\kappa_1 + \kappa_2}{2}. \quad (19)$$

The values of mean curvature provide the information of droplet interface, where the positive values of mean curvature indicate the convex interface and negative values indicate the concave interface as shown in Fig. 3d-f. In addition, there is a negative sign assigned to $\kappa_{Gi} A_i$ for concave interfaces and a value of 0 assigned for flat interfaces. Finally, we can obtain the macroscopic contact angle, θ_{macro}, for the droplet by normalizing the deficit curvature Θ as illustrated in Eq. (4),

$$\theta_{macro} = \lambda \Theta = \frac{4\pi - \sum \kappa_{Gi} A_i}{4N} \quad (20)$$

where N is the count of contact line loops. For more information, please see [16]. For multiphase systems where a large number of droplets are present, such as porous media and subsurface rocks, the proposed implementation procedure as described in Algorithm 1 enables the computation of macroscopic contact angles on a droplet-by-droplet basis.

4. Results and Discussion

4.1. Wetting in Flat and Ideally-smooth Surfaces

To unravel the effective and robust nature of the developed theory, we first compare the macroscopic contact angle θ_{macro} and the apparent microscopic contact angles θ_{app} on a flat and smooth surface. We performed a quasi-steady-state simulation of 3D sessile oil droplets immersed in immiscible ambient water on various flat surfaces that have different intrinsic contact angles defined by Young's equation. It is

a more ideal solution for performing simulation than experiments where the droplet after deposition achieves a different contact angle, i.e. wetting hysteresis, when compared to the intrinsic contact angle. This is due to the difficulties in attaining experimental equilibrium condition and collecting ideally-flat surface [41]. The equilibrium topologies of the oil droplets on the surface were simulated by minimizing the overall system energy and were subjected to constraints such as surface tension and gravitational energy. In the system, the overall energy is the sum of its interfacial potential energy and is governed by the Young-Laplace equation. For the interfacial potential energy of the droplet (E), it can be expressed as the sum of the respective interfacial energies,

$$E = \int\int_{A_{ls}} \sigma_{ls} dA + \int\int_{A_{lv}} \sigma_{lv} dA + \int\int_{A_{vs}} \sigma_{vs} dA, \quad (21)$$

where σ and A represent interfacial tension and interfacial area, respectively. By applying Young's equation, Eq. (21) becomes

$$\frac{E}{\sigma_{lv}} = A_{lv} - \int\int_{A_{ls}} \cos\theta_Y dA. \quad (22)$$

As shown in Fig. 5, the equilibrium topologies of oil droplets were simulated on a surface that gradually change from oleophobic to oleophilic. To obtain the microscopic apparent contact angles along the contact line, we implemented the 2D local method similar to [20] and the 3D local method developed by [21]. For the 2D local method, the contact points were smoothed using a moving average to determine the position and direction of the contact line. A 2D image was then extracted normal to the direction of the contact line for each contact point. In Fig. 4, we computed the contact angle measurement with different window (slice) sizes for each simulated droplet. The results demonstrate that a window (slice) size of 60 pixels is sufficient to provide an accurate contact angle. In contrast to [20], both circular and linear regressions were applied to best fit the solid surface. The best fit of either the circular or linear regression was determined by the lower of the two root-mean-square deviations. If the circle approximation was selected as the best fit, a line tangent to the circle at the contact point was calculated to represent the slope of the surface at that point. In addition, a constant curvature of the liquid/vapor interface was assumed under the assumption that the system is at equilibrium. Consequently, the apparent contact angle was measured as the angle between the solid surface and liquid/vapor interface tangent lines [42]. For the 3D local method, Gaussian smoothing was applied to the droplet surface. Then, the two vectors that have a direction perpendicular to liquid/vapor and liquid/solid interface were identified for each contact point along the contact line. The apparent contact angle was thereby computed from the dot product of these vectors.

In Fig. 5, we compare the macroscopic contact angle θ_{macro} distributions from the developed topological principle to the apparent contact angle distributions by the two
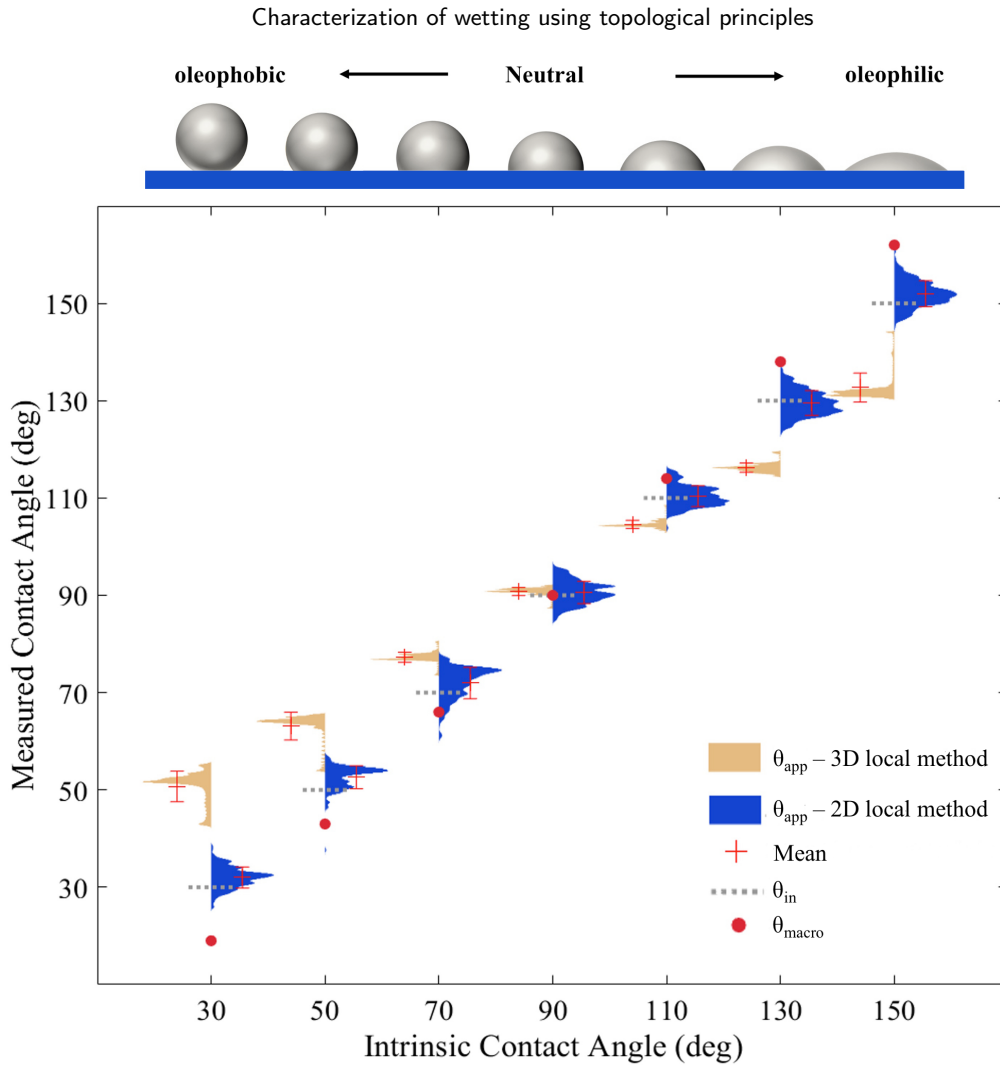
Fig. 5: The comparison diagram of θ_{macro} and the contact angle distributions of the 3D local measurement by [21] and modified 2D local measurement by [20] for the simulated droplets with different intrinsic contact angles.

local methods for each intrinsic contact angle. It is shown that the 2D local measurement has a higher standard deviation compared with the 3D local measurement. However, the mean values of the contact angle distribution for the 2D local measurement are closer to the intrinsic contact angle θ_{in}. Furthermore, the contact angle distribution calculated by 3D local method tends to have higher contact angles for more oleophobic surfaces and lower contact angles for more oleophilic surfaces, which provides a systematic bias (error) towards intermediate-wet conditions. Conversely, θ_{macro} is slightly less than the intrinsic contact angle for oleophobic surfaces and slightly greater than the intrinsic contact angle for oleophilic surfaces. The trend observed for θ_{macro} has a theoretical explanation since the total deficit curvature accounts for both local contact angles and the deformation of the contact line along the solid surface (line tension). The theoretical development for this particular aspect is explained in detail by Sun et al. [16]. Overall, contact angles measured for flat and homogeneous surfaces are comparable for all three tested methods, which supports the theoretical developments in Section 2.2 since the proposed topological

approach under these ideal conditions can be simplified to Young's equation.

4.2. Wetting in Complex Geometries

To further investigate the wetting state on heterogeneous surfaces where surface chemistry and roughness are present, we performed two quasi-static capillary forces dominated flow experiments for sintered glass at the Swiss Light Source and Bentheimer sandstone at the Australian National University [43]. The details of the experimental setup and image processing can be found in [44] and [16]. The sintered glass has a relatively lower degree of surface geometry with smooth surfaces and a lower degree of surface chemistry. While for Bentheimer sandstone, the surface chemical heterogeneity, surface geometry and roughness are relatively higher. In Table 1, a summary of experimental setup and image processing is given for both sintered glass and Bentheimer sandstone. The 3D fluid configurations and spatial arrangements for both samples are displayed in Figs. 7a and 8a.

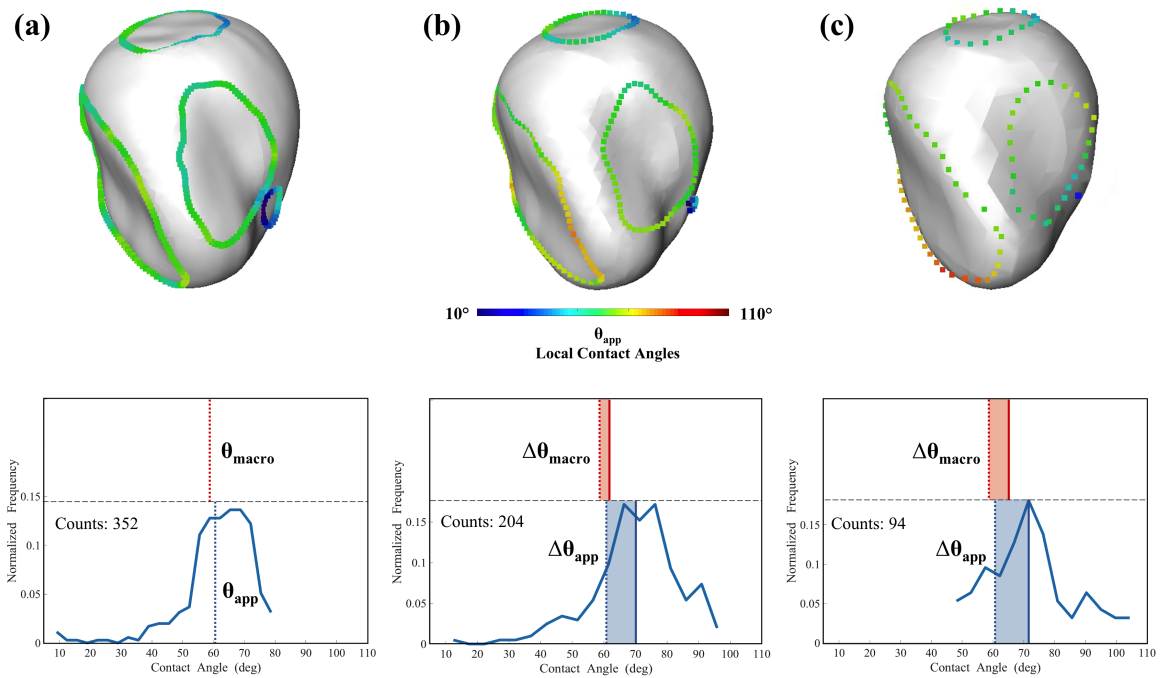To investigate the resolution effects, we first performed

Fig. 6: Top: The comparison of droplet topology as down-sampling the image resolution with measured local contact angles for each three-phase contact points. Bottom: The corresponding macroscopic contact angle (θ_{macro}) and 3D local measurements (θ_{app}) associated with their change by comparing with the original resolution. As deficit curvature is less sensitive to resolution effects, it is particularly attractive as a way to capture wetting on rough surfaces where sub-resolution heterogeneity can have a demonstrated influence on the measured macroscopic contact angle.

Table 1
Summary of experimental setup and image processing.

	Sintered Glass	Bentheimer Sandstone
Porosity	31.8%	24.1%
Permeability	21.5 ± 2 D	4.3 D
Sample diameter	4 mm	4.9 mm
Sample length	10 mm	10 mm
Non-wetting phase	n-decane	ambient air
Wetting phase	brine	brine
Injection rate	0.1 μL/min	0.3 μL/min
Brine saturation	78%	93%
Imaging source	fast synchrotron-based tomography	bench-top helical micro-tomography
Image resolution	4.2 μm	4.95 μm
Time step	30 s	1.35 hr

a resolution study by picking a well-resolved droplet from the dataset of Bentheimer sandstone. The original dimension of image for the droplet is $47 \times 51 \times 48$ voxels. We then down-sample the image of the droplet by halving the resolution twice as shown in Fig. 6a-c. It is intuitive in Fig. 6 how the down-sampling impacts the droplet interfacial curvature and contact line loops. The results demonstrate that the macroscopic contact angle based on the deficit curvature is less sensitive to resolution effects than local contact angle measurements, since the change in the mean value of θ_{app} is larger than the change in θ_{macro}. Local contact angle measurements cannot be performed without resolving the contact line region. It is clear that the resolution necessary to

measure the angles along the contact line is lost before the topological structure of the contact line loops is destroyed. In Fig. 6a-c, we investigate that the local contact angles vary significantly as the resolution decreases. For the topological approach based on the Gauss-Bonnet theorem, there remains a basis to obtain deficit curvature when the topological structure of the contact line loops is captured, even if only a single voxel represents the contact line loop as shown on the bottom right of Fig. 6c.

Further, we performed the contact angle distribution measurements for both samples on a collection of droplets by applying the topological approach for each droplet and 3D local method for each contact point. By gradually decreasing
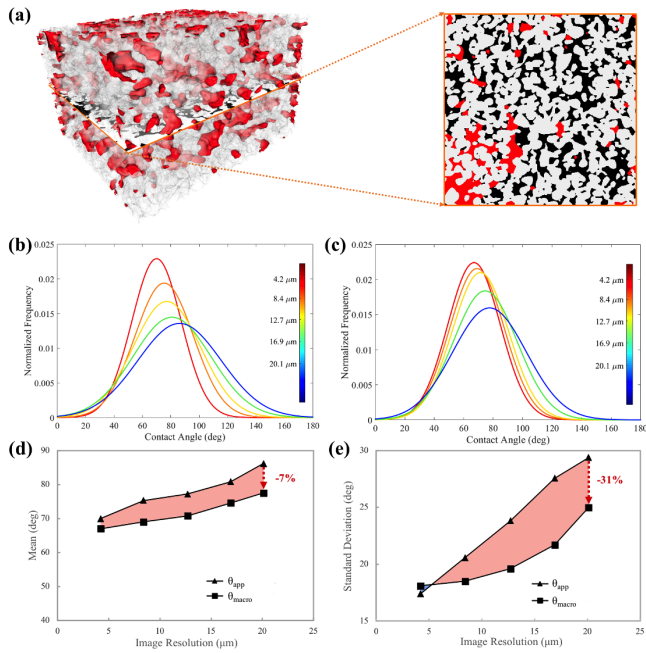
Fig. 7: The contact angle distributions of different image resolution for sintered glass by applying (b) 3D local method for each contact point and (c) the topological approach on a droplet-by-droplet basis. The plot of (d) mean and (e) standard deviation of the distribution for each image resolution.

Fig. 8: The contact angle distributions of different image resolution for Bentheimer sandstone by applying (b) 3D local method for each contact point and (c) the topological approach on a droplet-by-droplet basis. The plot of (d) mean and (e) standard deviation of the distribution for each image resolution.

the image resolution as shown in Figs. 7 and 8, the changes in the mean and standard deviation of the contact angle distributions for the topological approach are notably less than that of the local measurements. For sintered glass, the mean of the contact angle distribution decreases by an additional 7% while there is an additional 31% reduction in the standard deviation for the topological approach. Similar results for the topological method are investigated in the Bentheimer sandstone with a decrease in mean contact angle and standard deviation of 12% and 27%, respectively. Overall, at sufficiently high resolution, the topological approach and local measurements are comparable. While at lower resolutions, the topological approach deviates less from the high resolution results than the local contact angle measurements.

Lastly, we performed contact angle measurements for both samples by applying the topological approach, 2D and 3D local methods with the highest image resolution obtained as shown in Fig. 9. It reveals that the 2D local measurement provides a lower mean and a higher standard deviation of the contact angle distribution. However, the mean value of the 3D local measurement is the highest, which can be explained in the simulation of droplets results for the flat and homogeneous surfaces. For more oleophobic (water-wet) surfaces, contact angle measurements computed by the 3D local method is larger than the intrinsic contact angles. The θ_{macro} distribution computed by the topological approach falls between the two local methods. Overall, the topological and 3D local methods are comparable at sufficiently high resolution, suggesting that microscopic wetting
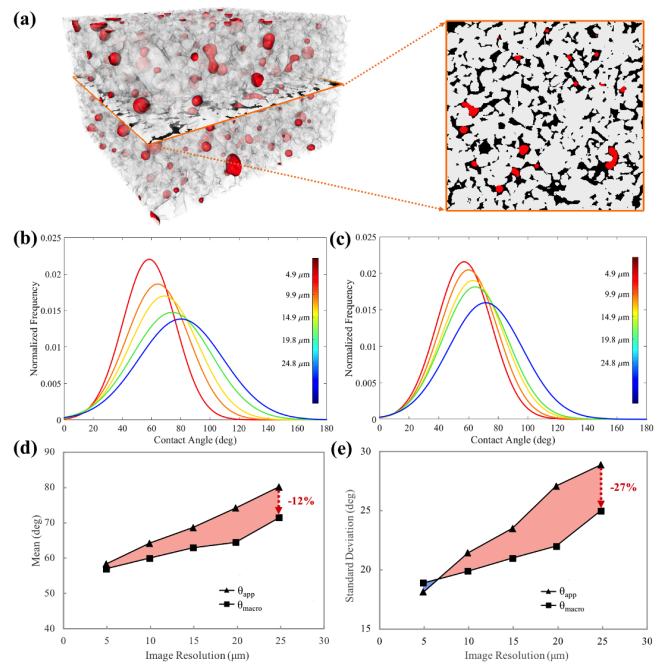
information is captured.

5. Conclusions

Recent methods for characterizing wetting behavior rely on restrictive thermodynamic laws such as Young's equation for flat homogeneous surfaces, and Wenzel and Cassie-Baxter models for heterogeneous surfaces [8, 9, 10]. In this work, we developed a new theory based on topological principles to determine the wetting state of multiphase systems. Specifically, the concept of thermodynamic equilibrium is not necessary since the formulation is a geometrical statement between the total surface curvature and global topology of a fluid object. In this regard, the proposed methodology does not require visualization of the three-phase contact line. It thus would be advantageous for applications where a large fluid body is resolved while the contact line pinning occurs at a smaller length scale. This could be particularly informative for problems where the droplet is connected to a thin film, such as a droplet slipping along a declining plane and/or the corner flow mechanism observed in porous media flows. We also highlight that the proposed theory is consistent with Young's equation for flat and homogeneous surfaces by performing a variational analysis.

By comparing with traditional local contact angle measurements [21, 20, 31], we assess the sensitivity and robustness of the proposed topological approach. It is found that the proposed theory has less sensitivity to resolution effects
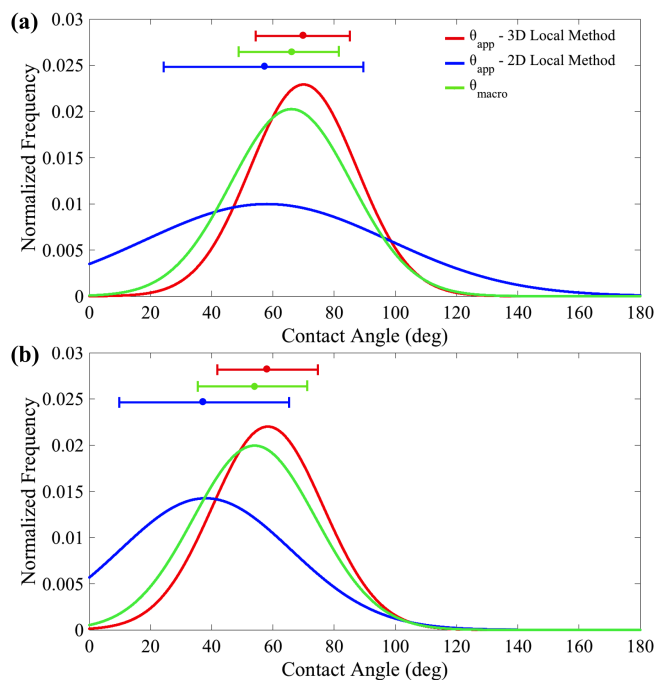
Fig. 9: The contact angle distributions for (a) sintered glass and (b) Bentheimer sandstone by applying topological approach, 2D and 3D local methods with the highest resolution obtained together with the associated mean and standard deviation.

than the tested local methods. While at sufficiently high image resolution, the results are comparable. As observed in Fig. 6, the resolution necessary to measure the contact line is lost before the topological structure of the contact line loops are destroyed. Contact angles cannot be measured without resolving the contact line region. However, the contact line region must always form a loop even if it is captured by only one voxel. Therefore, there remains a basis to measure θ_{macro} even at low image resolution since topology and interfacial curvatures of fluid surface are still captured. Another way to think about why θ_{macro} works well at low resolution is because fluid blobs are physically larger than the contact lines, and we can use information embedded in the fluid interface structure to infer the wetting state.

Overall, the results demonstrate that the proposed theory provides an accurate macroscopic wetting description based on microscopic wetting information that is less susceptible to resolution-based errors due to its robust nature of measuring interfacial area and curvature rather than angles along the contact line. The theoretical links of the proposed theory explored in other recent publications [37, 16] are further highlighted by the variational analysis presented herein. The particular example was provided for a simple sessile droplet system. However, more complex systems with morphologically and mineralogically heterogeneous geometries could be considered leading to a more general condition for the constrained entropy inequality. This could be particularly important for the development of multiphase flow models that explicitly account for wettability and will be the focus

of further work.

Acknowledgments

References

[1] P.-G. De Gennes, Wetting: statics and dynamics, Reviews of modern physics 57 (3) (1985) 827.
URL https://doi.org/10.1103/RevModPhys.57.827

[2] D. Bonn, J. Eggers, J. Indekeu, J. Meunier, E. Rolley, Wetting and spreading, Reviews of modern physics 81 (2) (2009) 739.
URL https://doi.org/10.1103/RevModPhys.81.739

[3] P.-G. De Gennes, F. Brochard-Wyart, D. Quéré, Capillarity and wetting phenomena: drops, bubbles, pearls, waves, Springer Science & Business Media, 2013.

[4] M. R. Powell, L. Cleary, M. Davenport, K. J. Shea, Z. S. Siwy, Electric-field-induced wetting and dewetting in single hydrophobic nanopores, Nature nanotechnology 6 (12) (2011) 798–802.
URL https://www.nature.com/articles/nnano.2011.189

[5] L.-C. Xu, J. W. Bauer, C. A. Siedlecki, Proteins, platelets, and blood coagulation at biomaterial interfaces, Colloids and Surfaces B: Biointerfaces 124 (2014) 49–68.
URL https://doi.org/10.1016/j.colsurfb.2014.09.040

[6] R. Blossey, Self-cleaning surfacesâĂŤvirtual realities, Nature materials 2 (5) (2003) 301.
URL https://www.nature.com/articles/nmat856

[7] W.-B. Bartels, H. Mahani, S. Berg, R. Menezes, J. A. van der Hoeven, A. Fadili, et al., Oil configuration under high-salinity and low-salinity conditions at pore scale: a parametric investigation by use of a single-channel micromodel, Spe Journal 22 (05) (2017) 1–362.

[8] T. Young, et al., Iii. an essay on the cohesion of fluids, Philosophical transactions of the royal society of London 95 (1805) 65–87.
URL https://doi.org/10.1098/rstl.1805.0005

[9] R. N. Wenzel, Resistance of solid surfaces to wetting by water, Industrial & Engineering Chemistry 28 (8) (1936) 988–994.
URL https://pubs.acs.org/doi/pdf/10.1021/ie50320a024

[10] A. Cassie, S. Baxter, Wettability of porous surfaces, Transactions of the Faraday society 40 (1944) 546–551.
URL http://doi.org/10.1039/TF9444000546

[11] E. Decker, S. Garoff, Contact line structure and dynamics on surfaces with contact angle hysteresis, Langmuir 13 (23) (1997) 6321–6332.

[12] D. I. Yu, S. W. Doh, H. J. Kwak, H. C. Kang, H. S. Ahn, H. S. Park, M. Kiyofumi, M. H. Kim, Wetting state on hydrophilic and hydrophobic micro-textured surfaces: Thermodynamic analysis and x-ray visualization, Applied Physics Letters 106 (17) (2015) 171602.
URL https://doi.org/10.1063/1.4919136

[13] M. Turmine, P. Letellier, Thermodynamic approach to the wetting of solids by surface-active agents: A supplementary approach to the gibbs formalism, Journal of colloid and interface science 227 (1) (2000) 71–77.
URL https://doi.org/10.1006/jcis.1999.6865

[14] M. J. Blunt, Q. Lin, T. Akai, B. Bijeljic, A thermodynamically consistent characterization of wettability in porous media using high-

resolution imaging, Journal of colloid and interface science 552 (2019) 59–65.
URL https://doi.org/10.1016/j.jcis.2019.05.026

[15] H. Mahani, S. Berg, D. Ilic, W.-B. Bartels, V. Joekar-Niasar, et al., Kinetics of low-salinity-flooding effect, Spe Journal 20 (01) (2015) 8–20.

[16] C. Sun, J. E. McClure, P. Mostaghimi, A. L. Herring, S. Berg, R. T. Armstrong, Probing effective wetting in subsurface systems, Geophysical Research Letters (2020).
URL https://doi.org/10.1029/2019GL086151

[17] R. Holtzman, E. Segre, Wettability stabilizes fluid invasion into porous media via nonlocal, cooperative pore filling, Physical review letters 115 (16) (2015) 164501.
URL https://doi.org/10.1103/PhysRevLett.115.164501

[18] G. Garfi, C. M. John, Q. Lin, S. Berg, S. Krevor, Fluid surface coverage showing the controls of rock mineralogy on the wetting state, Geophysical Research Letters (2019).

[19] D. Kwok, T. Gietzelt, K. Grundke, H.-J. Jacobasch, A. W. Neumann, Contact angle measurements and contact angle interpretation. 1. contact angle measurements by axisymmetric drop shape analysis and a goniometer sessile drop technique, Langmuir 13 (10) (1997) 2880–2894.

[20] A. Scanziani, K. Singh, M. J. Blunt, A. Guadagnini, Automatic method for estimation of in situ effective contact angle from x-ray micro tomography images of two-phase flow in porous media, Journal of colloid and interface science 496 (2017) 51–59.
URL https://doi.org/10.1016/j.jcis.2017.02.005

[21] A. AlRatrout, A. Q. Raeini, B. Bijeljic, M. J. Blunt, Automatic measurement of contact angle in pore-space images, Advances in water resources 109 (2017) 158–169.
URL https://doi.org/10.1016/j.advwatres.2017.07.018

[22] A. Ibekwe, D. Pokrajac, Y. Tanino, Automated extraction of in situ contact angles from micro-computed tomography images of porous media, Computers & Geosciences 137 (2020) 104425.

[23] L. E. Dalton, K. A. Klise, S. Fuchs, D. Crandall, A. Goodman, Methods to measure contact angles in scco2-brine-sandstone systems, Advances in Water Resources 122 (2018) 278–290.

[24] D. Wildenschild, A. P. Sheppard, X-ray imaging and analysis techniques for quantifying pore-scale structure and processes in subsurface porous medium systems, Advances in Water Resources 51 (2013) 217–246.

[25] M. Sundberg, A. Månsson, S. Tågerud, Contact angle measurements by confocal microscopy for non-destructive microscale surface characterization, Journal of colloid and interface science 313 (2) (2007) 454–460.

[26] M. Andrew, B. Bijeljic, M. J. Blunt, Pore-scale contact angle measurements at reservoir conditions using x-ray microtomography, Advances in Water Resources 68 (2014) 24–31.
URL https://doi.org/10.1016/j.advwatres.2014.02.014

[27] A. AlRatrout, M. J. Blunt, B. Bijeljic, Wettability in complex porous materials, the mixed-wet state, and its relationship to surface roughness, Proceedings of the National Academy of Sciences 115 (36) (2018) 8901–8906.
URL https://doi.org/10.1073/pnas.1803734115

[28] J. Tudek, D. Crandall, S. Fuchs, C. J. Werth, A. J. Valocchi, Y. Chen, A. Goodman, In situ contact angle measurements of liquid co2, brine, and mount simon sandstone core using micro x-ray ct imaging, sessile drop, and lattice boltzmann modeling, Journal of Petroleum Science and Engineering 155 (2017) 3–10.

[29] S. Schlüter, A. Sheppard, K. Brown, D. Wildenschild, Image processing of multiphase images obtained via x-ray microtomography: a review, Water Resources Research 50 (4) (2014) 3615–3639.

[30] R. T. Armstrong, M. L. Porter, D. Wildenschild, Linking pore-scale interfacial curvature to column-scale capillary pressure, Advances in Water Resources 46 (2012) 55–62.
URL https://doi.org/10.1016/j.advwatres.2012.05.009

[31] K. A. Klise, D. Moriarty, H. Yoon, Z. Karpyn, Automated contact angle estimation for three-dimensional x-ray microtomography data,

Advances in water resources 95 (2016) 152–160.
URL https://doi.org/10.1016/j.advwatres.2015.11.006

[32] R. E. Johnson Jr, R. H. Dettre, Contact angle hysteresis. iii. study of an idealized heterogeneous surface, The journal of physical chemistry 68 (7) (1964) 1744–1750.
URL https://pubs.acs.org/doi/pdf/10.1021/j100789a012

[33] N. R. Morrow, et al., The effects of surface roughness on contact: angle with special reference to petroleum recovery, Journal of Canadian Petroleum Technology 14 (04) (1975).
URL https://doi.org/10.2118/75-04-04

[34] C. Priest, R. Sedev, J. Ralston, Asymmetric wetting hysteresis on chemical defects, Physical review letters 99 (2) (2007) 026103.
URL https://doi.org/10.1103/PhysRevLett.99.026103

[35] J. Indekeu, Line tension at wetting, International Journal of Modern Physics B 8 (03) (1994) 309–345.
URL https://doi.org/10.1142/S0217979294000129

[36] H. S. Rabbani, B. Zhao, R. Juanes, N. Shokri, Pore geometry control of apparent wetting in porous media, Scientific reports 8 (1) (2018) 1–8.

[37] C. Sun, J. E. McClure, P. Mostaghimi, A. L. Herring, M. Shabaninejad, S. Berg, R. T. Armstrong, Linking continuum-scale state of wetting to pore-scale contact angles in porous media, Journal of Colloid and Interface Science 561 (2020) 173–180.
URL https://doi.org/10.1016/j.jcis.2019.11.105

[38] S.-s. Chern, A simple intrinsic proof of the gauss-bonnet formula for closed riemannian manifolds, Annals of mathematics (1944) 747–752.
URL https://www.jstor.org/stable/1969302

[39] K. Seo, M. Kim, et al., Re-derivation of youngâĂŹs equation, wenzel equation, and cassie-baxter equation based on energy minimization, in: Surface Energy, InTechOpen, 2015.

[40] H.-C. Hege, M. Seebass, D. Stalling, M. Zöckler, A generalized marching cubes algorithm based on non-binary classifications (1997).

[41] O. Arjmandi-Tash, N. M. Kovalchuk, A. Trybala, I. V. Kuchin, V. Starov, Kinetics of wetting and spreading of droplets over various substrates, Langmuir 33 (18) (2017) 4367–4385.

[42] D. E. MEISENHEIMER, M. L. RIVERS, D. WILDENSCHILD, Optimizing pink-beam fast x-ray microtomography for multi-phase flow in 3d porous media, Journal of Microscopy (2020).

[43] C. Sun, J. Mcclure, P. Mostaghimi, A. Herring, S. Berg, R. Armstrong, Bentheimer sandstone for analyzing wetting phenomena, http://www.digitalrocksportal.org/projects/236 (2019). doi:10.17612/P8FQ-6Y93.

[44] S. Schlüter, S. Berg, M. Rücker, R. Armstrong, H.-J. Vogel, R. Hilfer, D. Wildenschild, Pore-scale displacement mechanisms as a source of hysteresis for two-phase flow in porous media, Water Resources Research 52 (3) (2016) 2194–2205.